

Deeply Virtual Compton Scattering off the Neutron

M. Mazouz,¹ A. Camsonne,² C. Muñoz Camacho,³ C. Ferdi,² G. Gavalian,⁴ E. Kuchina,⁵ M. Amarian,⁴ K. A. Aniol,⁶ M. Beaumel,³ H. Benaoum,⁷ P. Bertin,^{2,8} M. Brossard,² J.-P. Chen,⁸ E. Chudakov,⁸ B. Craver,⁹ F. Cusanno,¹⁰ C.W. de Jager,⁸ A. Deur,⁸ R. Feuerbach,⁸ J.-M. Fieschi,² S. Frullani,¹⁰ M. Garçon,³ F. Garibaldi,¹⁰ O. Gayou,¹¹ R. Gilman,⁵ J. Gomez,⁸ P. Gueye,¹² P.A.M. Guichon,³ B. Guillon,¹ O. Hansen,⁸ D. Hayes,⁴ D. Higinbotham,⁸ T. Holmstrom,¹³ C.E. Hyde,^{2,4} H. Ibrahim,⁴ R. Igarashi,¹⁴ X. Jiang,⁵ H.S. Jo,¹⁵ L.J. Kaufman,¹⁶ A. Kelleher,¹³ A. Kolarkar,¹⁷ G. Kumbartzki,⁵ G. Laveissiere,² J.J. LeRose,⁸ R. Lindgren,⁹ N. Liyanage,⁹ H.-J. Lu,¹⁸ D.J. Margaziotis,⁶ Z.-E. Meziani,¹⁹ K. McCormick,⁵ R. Michaels,⁸ B. Michel,² B. Moffit,¹³ P. Monaghan,¹¹ S. Nanda,⁸ V. Nelyubin,⁹ M. Potokar,²⁰ Y. Qiang,¹¹ R.D. Ransome,⁵ J.-S. Réal,¹ B. Reitz,⁸ Y. Roblin,⁸ J. Roche,⁸ F. Sabatié,³ A. Saha,⁸ S. Sirca,²⁰ K. Slifer,⁹ P. Solvignon,¹⁹ R. Subedi,²¹ V. Sulkosky,¹³ P.E. Ulmer,⁴ E. Voutier,¹ K. Wang,⁹ L.B. Weinstein,⁴ B. Wojtsekhowski,⁸ X. Zheng,²² and L. Zhu²³

(The Jefferson Lab Hall A Collaboration)

¹*LPSC, Université Joseph Fourier, CNRS/IN2P3, INPG, F-38026 Grenoble, France*

²*LPC Clermont-Ferrand, Université Blaise Pascal, CNRS/IN2P3, F-63177 Aubière, France*

³*CEA Saclay, DAPNIA/SPhN, F-91191 Gif-sur-Yvette, France*

⁴*Old Dominion University, Norfolk, Virginia 23508, USA*

⁵*Rutgers, The State University of New Jersey, Piscataway, New Jersey 08854, USA*

⁶*California State University, Los Angeles, Los Angeles, California 90032, USA*

⁷*Syracuse University, Syracuse, New York 13244, USA*

⁸*Thomas Jefferson National Accelerator Facility, Newport News, Virginia 23606, USA*

⁹*University of Virginia, Charlottesville, Virginia 22904, USA*

¹⁰*INFN/Sezione Sanità, 00161 Roma, Italy*

¹¹*Massachusetts Institute of Technology, Cambridge, Massachusetts 02139, USA*

¹²*Hampton University, Hampton, Virginia 23668, USA*

¹³*College of William and Mary, Williamsburg, Virginia 23187, USA*

¹⁴*University of Saskatchewan, Saskatchewan, SK, Canada, S7N 5C6*

¹⁵*IPN Orsay, Université Paris Sud, CNRS/IN2P3, F-91406 Orsay, France*

¹⁶*University of Massachusetts Amherst, Amherst, Massachusetts 01003, USA*

¹⁷*University of Kentucky, Lexington, Kentucky 40506, USA*

¹⁸*Department of Modern Physics, University of Science and Technology of China, Hefei 230026, China*

¹⁹*Temple University, Philadelphia, Pennsylvania 19122, USA*

²⁰*Institut Jozef Stefan, University of Ljubljana, Ljubljana, Slovenia*

²¹*Kent State University, Kent, Ohio 44242, USA*

²²*Argonne National Laboratory, Argonne, Illinois, 60439, USA*

²³*University of Illinois, Urbana, Illinois 61801, USA*

The present experiment exploits the interference between the Deeply Virtual Compton Scattering (DVCS) and the Bethe-Heitler processes to extract the imaginary part of DVCS amplitudes on the neutron and on the deuteron from the helicity-dependent $D(\vec{e}, e'\gamma)X$ cross section measured at $Q^2=1.9 \text{ GeV}^2$ and $x_B=0.36$. We extract a linear combination of generalized parton distributions (GPDs) particularly sensitive to E_q , the least constrained GPD. A model dependent constraint on the contribution of the up and down quarks to the nucleon spin is deduced.

PACS numbers: 13.60.Fz, 13.85.Hd, 14.20.Dh, 14.65.-q

Understanding the structure of the nucleon in terms of quarks and gluons is a central project of modern hadronic physics. In the non-perturbative regime relevant to nuclear scales, Quantum Chromodynamics (QCD), the theory describing the elementary dynamics of the nucleon, is not yet solvable and remains rather mysterious. The electromagnetic probe provides an outstanding tool to study the nucleon structure. In this letter, we present the first study of the $(\vec{e}, e'\gamma)$ reaction on neutrons off a deuterium target.

Elastic electron scattering revealed the non-pointlike nature of the nucleon [1]. Deviations from the Mott cross

section define the electromagnetic form factors which describe the spatial distribution of charge and current inside the nucleon, as functions of the invariant momentum transfer squared (Q^2), i.e. the resolution of the probe. Deep Inelastic Scattering (DIS) revealed the partons inside the nucleon [2]. The DIS cross section can be expressed in terms of the probability to find a quark with fraction x_B of the nucleon longitudinal momentum. This motivated extensive measurements of the momentum distribution of quarks and gluons in nucleons, i.e. the parton distributions. Polarized DIS with longitudinally polarized beams and targets measures the probability to find

a parton of given momentum with spin aligned or anti-aligned with the proton spin. These experiments yielded the unexpected result that the quarks carried about only 30% of the total spin of the nucleon [3] and questioned the role of gluons in this puzzle. Experimental results to date suggest that the gluon polarization does not contribute significantly to the nucleon spin [4, 5]. A natural candidate to solve this problem is the orbital angular momentum of quarks and gluons.

The Generalized Parton Distribution (GPD) framework provides a new formalism to unravel the nucleon structure that unifies form factors, parton distributions, and the angular momentum of partons [6, 7, 8]. Quark GPDs are four universal functions H_q , E_q , \tilde{H}_q , and \tilde{E}_q , defined by the nucleon helicity-conserving and helicity-flip matrix elements of the vector and axial-vector currents for quark flavor q . The GPDs correspond to the amplitude for removing a parton of momentum fraction $x + \xi$ and restoring it with momentum fraction $x - \xi$ (Fig. 1). In this process, the nucleon receives an invariant momentum transfer $t = \Delta^2$. In impact parameter space, the transverse momentum transfer Δ_\perp is Fourier conjugate to the transverse position of the parton leading to a femto-tomography [9, 10, 11, 12] of the nucleon: GPDs represent distributions, in the transverse plane, of partons carrying longitudinal momentum x . The correlation of the position and momentum of quarks can exactly be combined into an orbital momentum [13]. This is explicit in Ji's sum rule [8]

$$\begin{aligned} J_q &= \frac{1}{2} \Delta \Sigma_q + L_q \\ &= \frac{1}{2} \int_{-1}^{+1} dx x [H_q(x, \xi, t=0) + E_q(x, \xi, t=0)] \end{aligned} \quad (1)$$

which is independent of the ξ -value. Polarized DIS measures the spin part $\Delta \Sigma_q$, and unpolarized DIS determines the momentum sum rule and forward limit of H_q

$$M_q = \int_{-1}^{+1} dx x q(x) = \int_{-1}^{+1} dx x H_q(x, \xi = 0, t = 0) \quad (2)$$

meaning that the contribution of H_q to Eq. 1 is known. Constraints on E_q will allow access to the quark orbital momentum in the nucleon.

Deeply virtual Compton scattering (DVCS) is the simplest reaction to access GPDs (Fig. 1). In the Bjorken limit, similar to DIS, where $-t \ll Q^2$ and Q^2 is much larger than the quark confinement scale, the factorization theorem separates the reaction amplitude into the convolution of a known perturbative $\gamma^* q \rightarrow \gamma q$ kernel with an unknown soft matrix element describing the nucleon structure (GPDs) [14, 15]. The Bethe-Heitler (BH) process, where the real photon is emitted by either the incoming or scattered electrons, serves as a reference amplitude that interferes with the Compton amplitude. The difference between polarized cross sections for opposite

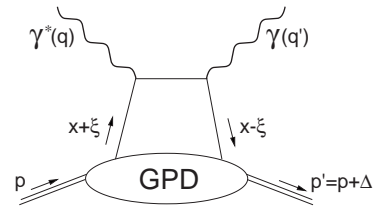


FIG. 1: Lowest order (QCD) amplitude for the virtual Compton process. The momentum four-vectors of the incident and scattered photon are q and q' , respectively. The momentum four-vectors of the initial and final proton are p and p' , with $\Delta = (p' - p) = (q - q')$. The DIS scaling variable is $x_B = Q^2 / (2p \cdot q)$ and the DVCS scaling variable is $\xi = x_B / (2 - x_B)$. In light cone coordinates defined by $P = (p + p')/2$, the initial and final momentum of the photons are -2ξ and 0 , respectively.

beam longitudinal polarization isolates, at leading order in $1/Q$, the imaginary part of the interference between the BH and DVCS amplitudes [16]. This difference is a direct measurement of a linear combination of GPDs [17] dominated by the contribution of E_q in the neutron case.

The first evidence for DVCS was reported in beam-helicity asymmetries at HERMES [18], and CLAS [19], and in unpolarized cross sections at HERA [20, 21, 22], and more recently in measurements of the target spin asymmetry [23] and beam charge asymmetry [24]. A dedicated $H(\vec{e}, e' \gamma) p$ experiment in Jefferson Laboratory (JLab) Hall A shows evidence for factorization at Q^2 as low as 2.0 GeV² [25]. The E03-106 experiment [26] reported here is an exploratory experiment investigating for the first time the DVCS reaction off the neutron.

The experimental data were acquired in JLab Hall A, consecutively to the $H(\vec{e}, e' \gamma) p$ experiment. A 5.75 GeV/c longitudinally polarized electron beam impinged on a 15 cm liquid D₂ cell serving as quasi-free neutron target. Scattered electrons of 2.94 GeV/c were detected at 19.3° in the left High Resolution Spectrometer (HRS-L) [27] selecting kinematics at $Q^2 = 1.9$ GeV² and $x_B = 0.36$. DVCS photons were detected in a PbF₂ electromagnetic calorimeter organized in an 11 × 12 array of 3 × 3 × 18.6 cm³ crystals centered around the direction of the virtual photon at -18.3°. The calorimeter front face was 110 cm from the target center covering a t acceptance $-0.5 \text{ GeV}^2 < t$. Typical beam intensities of 4 μA yielded a $4 \times 10^{37} \text{ cm}^{-2} \cdot \text{s}^{-1}$ /nucleon luminosity with 76% polarized electrons. Three independent reactions are used to calibrate and monitor the calorimeter: $H(e, e'_{\text{Calo}}, p_{\text{HRS}})$, $D(e, e'_{\text{Calo}}, \pi_{\text{HRS}}^-) pp$, and $H, D(e, e'_{\text{HRS}}, \pi_{\text{Calo}}^0) X$ [28]. Recoil particle detection in the HRS provides tagged electrons in the calorimeter allowing for the independent calibration of each block. The mass and width of the π^0 peak reconstructed from the invariant mass of $\gamma\gamma$ events in the calorimeter provide independent tests of the previous calibrations. π_{HRS}^- and π_{Calo}^0 data have been taken simultaneously with DVCS data, ensuring a continuous monitor-

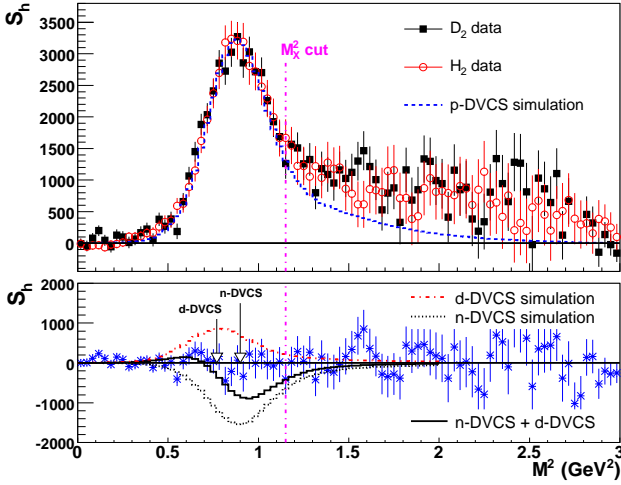


FIG. 2: (top) Helicity signal (Eq. 4) for $D(e, e'\gamma)X$ and $H(e, e'\gamma)X$ events; H_2 data are folded with a momentum distribution of the proton in deuterium, and scaled to the D_2 data luminosity; the simulation curve is for the Fermi broadened $H(e, e'\gamma)p$ reaction. (bottom) Residual helicity signal after H_2 subtraction; the arrows indicate the M_X^2 average position of n-DVCS and d-DVCS events for $\langle t \rangle = -0.3 \text{ GeV}^2$; the simulation curves, integrated over the complete experimental acceptance and obtained for the arbitrary values $\Im m [C_n^I]^{exp} = -\Im m [C_d^I]^{exp} = -1$ (Eq. 5), illustrate the sensitivity of the data to the neutron and deuteron signals.

ing of the calibration and the resolution of the calorimeter. A 1% uncertainty on the calorimeter calibration was estimated from the differences between π^- and π^0 calibrations. The final state of the $D(\bar{e}, e'\gamma)X$ reaction was selected via the squared missing mass $M_X^2 = (q + p - q')^2$ reconstructed from the virtual and real photons.

The three-momentum transfer $|\vec{\Delta}|$ to the target varies within 0.4-0.8 GeV/c in our acceptance. In this range, the impulse approximation (IA) is expected to accurately describe the inclusive yield. Within the IA, the cross section for electroproduction of photons on a deuterium target may be decomposed into elastic (d-DVCS) and quasi-elastic (p-DVCS and n-DVCS) contributions following

$$D(\bar{e}, e'\gamma)X = d(\bar{e}, e'\gamma)d + n(\bar{e}, e'\gamma)n + p(\bar{e}, e'\gamma)p + \dots \quad (3)$$

where meson production channels are also contributing as background. Cross sections are obtained from $D(\bar{e}, e'\gamma)X$ events after subtraction of the proton quasi-elastic contribution deduced from measurements on a liquid H_2 target: the Fermi motion of bound protons is statistically added to the squared missing mass $M_X^2|_0$ of free proton data following $M_X^2 = M_X^2|_0 - 2\vec{p}_i \cdot (\vec{q} - \vec{q}')$ where \vec{p}_i is the initial proton momentum in the deuteron from [29]; this leads to a 3% relative increase of the M_X^2 spectrum resolution.

The helicity signal (S_h) is defined according to

$$S_h = \int_0^\pi (N^+ - N^-) d^5\Phi - \int_\pi^{2\pi} (N^+ - N^-) d^5\Phi \quad (4)$$

where $d^5\Phi = dQ^2 dx_B dt d\phi_e d\phi_{\gamma\gamma}$ is the detection hyper-volume; the integration boundaries in Eq. 4 define the limits in the azimuthal angle $\phi_{\gamma\gamma}$ [30]; N^\pm are the number of counts for \pm beam helicity, corrected for random coincidences, and integrated over a particular bin in M_X^2 . The helicity signal for D_2 and H_2 targets from $(\bar{e}, e'\gamma)$ coincident detection is displayed in Fig. 2 (top) as a function of the squared missing mass. For our purposes, M_X^2 is calculated with a target corresponding to a nucleon at rest, leading to the kinematic $\Delta M_X^2 \simeq t/2$ separation between deuteron elastic and nucleon quasi-elastic contributions. Pion production channels ($eA \rightarrow eA\gamma\pi$, $eA \rightarrow eA\pi^0\pi \dots$) are strongly suppressed by the kinematical constraint $M_X^2 < (M + m_\pi)^2 = M_X^2|_{cut}$. Their contribution to the helicity signal of p-DVCS, induced via resolution effects below $M_X^2|_{cut}$, was found to be negligible on the proton as illustrated by the comparison between H_2 data and scaled simulations (Fig. 2 top). Figure 2 (bottom) shows the subtraction ($D-H$ data) of the two spectra of Fig. 2 (top). The residual helicity signal for $M_X^2 < M_X^2|_{cut}$ is compatible with zero. It corresponds to the sum of the coherent d-DVCS and incoherent n-DVCS processes (Eq. 3). Asymmetric decays of π^0 (in $eA \rightarrow eA\pi^0$), where only one photon is detected in the calorimeter, mimic DVCS events. The contamination due to this background was treated as a systematic error estimated from the number of detected π^0 events, corresponding to primarily symmetric decays [25].

The H_2 results [25] show that the handbag mechanism (Fig. 1) dominates the p-DVCS helicity-dependent cross section difference at our kinematics. As a consequence, only twist-2 contributions are considered in this analysis. The *exp* superscript in Eq. 5 reflects this restriction. In the impulse approximation, we write the experimental helicity-dependent cross-section difference as the sum of the (incoherent) neutron and the (coherent) deuteron contributions, within the formalism of Refs. [17, 31]

$$\begin{aligned} \frac{d^5\Sigma_{D-H}}{d^5\Phi} &= \frac{1}{2} \left[\frac{d^5\sigma^+}{d^5\Phi} - \frac{d^5\sigma^-}{d^5\Phi} \right] \\ &= \left(\Gamma_d^\Im \Im m [C_d^I]^{exp} + \Gamma_n^\Im \Im m [C_n^I]^{exp} \right) \sin(\phi_{\gamma\gamma}). \end{aligned} \quad (5)$$

$\Gamma_{n,d}^\Im$ are kinematical factors with a $\phi_{\gamma\gamma}$ dependence that arises from the electron propagators of the BH amplitude; in the t range of interest, the averaged $\Gamma_n^\Im/\Gamma_d^\Im$ ratio vary from 0.4 to 0.9 with increasing $|t|$. $\Im m [C_n^I]$ depends on the interference of the BH amplitude with the set $\mathcal{F} = \{\mathcal{H}, \mathcal{E}, \tilde{\mathcal{H}}\}$ of twist-2 Compton form factors (CFFs):

$$[C_n^I]^{exp} \simeq [C_n^I] = F_1 \mathcal{H} + \xi(F_1 + F_2) \tilde{\mathcal{H}} - \frac{t}{4M^2} F_2 \mathcal{E} \quad (6)$$

where F_1 (F_2) is the Dirac (Pauli) form factor entering into the BH amplitude. Similarly, $\Im m [C_d^I]$ depends on the different set of spin-1 CFFs of the deuteron [31]. The imaginary part of twist-2 CFFs is determined by the $x =$

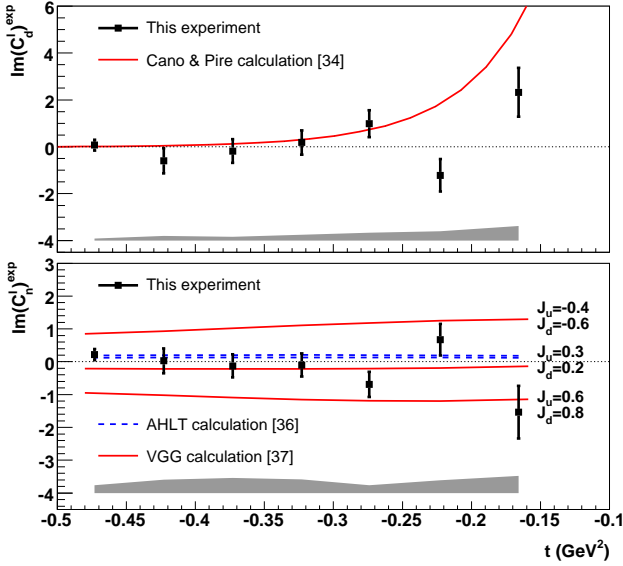


FIG. 3: The t -dependence of the extracted $\sin(\phi_{\gamma\gamma})$ moments for coherent d-DVCS (top panel) and incoherent n-DVCS (bottom panel). Error bars show statistical uncertainties; systematical uncertainties are indicated by the shaded bands.

$\pm\xi$ points of the GPDs, with for example:

$$\Im m[\mathcal{E}] = \pi \sum_q e_q^2 (E_q(\xi, \xi, t) - E_q(-\xi, \xi, t)) . \quad (7)$$

where e_q is the quark charge in units of the elementary charge. While Eq. 6 for a proton is dominated by \mathcal{H} and $\tilde{\mathcal{H}}$, it becomes essentially sensitive to \mathcal{E} in the neutron case following the small value of F_1 and the cancellation between u and d polarized parton distributions in $\tilde{\mathcal{H}}$ [32].

$\Im m[\mathcal{C}_n^I]^{exp}$ and $\Im m[\mathcal{C}_d^I]^{exp}$ are simultaneously extracted in each t -bin from a global analysis involving $7 \times 12 \times 30$ bins in $t \otimes \phi_{\gamma\gamma} \otimes M_X^2 \in [-0.5; -0.1] \text{ GeV}^2 \otimes [0; 2\pi] \otimes [0; 1.15] \text{ GeV}^2$. A Monte Carlo simulation with the kinematic weights of Eq. 5 as a function of $(t, \phi_{\gamma\gamma}, M_X^2)$ is fitted to the experimental distribution $[N^+(t, \phi_{\gamma\gamma}, M_X^2) - N^-(t, \phi_{\gamma\gamma}, M_X^2)]$ obtained after the D–H subtraction. The two coefficients $\Im m[\mathcal{C}_n^I(t_i)]^{exp}$ and $\Im m[\mathcal{C}_d^I(t_i)]^{exp}$ are the free parameters of the fit in each bin t_i . The binning in $\phi_{\gamma\gamma}$ allows the determination of the $\sin(\phi_{\gamma\gamma})$ moments whereas the binning in M_X^2 allows the separation of the d-DVCS and n-DVCS signals. The simulation includes both external and real internal radiative effects. It takes also into account detector resolution and acceptance. Finally, virtual and soft real radiative corrections are applied with a global correction factor of 0.91 ± 0.02 to the experimental yields [33].

Figure 3 displays the experimental values (Tab. I) of $\Im m[\mathcal{C}_{n,d}^I(t_i)]^{exp}$. At low $|t|$, the small kinematic separation between d-DVCS and n-DVCS leads to a strong anti-correlation between deuteron and neutron moments

$\langle t \rangle$	$\Im m[\mathcal{C}_n^I(t_i)]^{exp}$	$\Im m[\mathcal{C}_d^I(t_i)]^{exp}$	α_{nd}
-0.473	$0.22 \pm 0.17 \pm 0.24$	$0.07 \pm 0.23 \pm 0.08$	-0.72
-0.423	$0.03 \pm 0.38 \pm 0.41$	$-0.60 \pm 0.54 \pm 0.19$	-0.77
-0.373	$-0.13 \pm 0.35 \pm 0.46$	$0.18 \pm 0.51 \pm 0.17$	-0.80
-0.323	$-0.10 \pm 0.35 \pm 0.42$	$0.18 \pm 0.52 \pm 0.24$	-0.84
-0.274	$-0.69 \pm 0.38 \pm 0.24$	$0.98 \pm 0.57 \pm 0.33$	-0.88
-0.225	$0.67 \pm 0.48 \pm 0.39$	$-1.22 \pm 0.69 \pm 0.40$	-0.91
-0.166	$-1.54 \pm 0.80 \pm 0.52$	$2.32 \pm 1.04 \pm 0.61$	-0.95

TABLE I: Experimental values of the $\sin(\phi_{\gamma\gamma})$ moments as a function of t (in GeV^2). The first error is statistical and the second is the total systematic one resulting from the quadratic sum of each contribution; α_{nd} is the correlation coefficient between the two extracted moments.

(Tab. I). The larger statistical errors on the extraction at low $|t|$, in spite of higher absolute statistics, reflect this feature. The systematical errors come essentially from the t -dependent uncertainties on the relative calibration between D_2 and H_2 data, and estimates of the bound on π^0 contamination; other contributions originate from DVCS detectors acceptance and luminosity (3%), beam polarization (2%) and radiative corrections (2%). As expected from Fig. 2, the moments are globally compatible with zero. Experimental results are compared to model calculations for deuteron [34, 35] and neutron [36, 37] GPDs. The deuteron calculations exhibit a rapid decrease of the deuteron form factors with $|t|$. The n-DVCS results are compared to two different models: one where the GPDs parametrization is constrained by lattice calculation of GPDs moments [36], and another where E_q is parametrized by the unknown contribution of valence quarks to the nucleon angular momentum [32]. Both approaches reproduce the rather flat t -dependence of the data. Three examples of calculations corresponding to different values of the u (J_u) and d (J_d) quark contributions are shown. This comparison indicates that the present data provide constraints of the GPD models, particularly on E_q .

A correlated constraint on J_u and J_d can be extracted from a fit of the VGG model [32, 37] to the neutron data (Fig. 3), relying on the χ^2 quantity

$$\chi^2 = \sum_{i=1}^7 \frac{\left(\Im m[\mathcal{C}_n^I(t_i)]^{exp} - \Im m[\mathcal{C}_n^I(t_i)]_{J_u, J_d}^{VGG} \right)^2}{(\delta_{stat}^{exp})^2 + (\delta_{sys}^{exp})^2} . \quad (8)$$

The condition $\chi^2 \leq \chi_{min}^2 + 1$ ($\chi_{min}^2/\text{DoF}=6.6/5$) defines the band $J_d + (J_u/5.0) = 0.18 \pm 0.14$ of Fig. 4. The model dependence of this analysis should be stressed: n-DVCS data involve GPDs at one point $x=\pm\xi$ and $t \neq 0$ while the Ji sum rule (Eq. 1) is an integral over x extrapolated to $t=0$. A similar constraint obtained from HERMES preliminary \bar{p} -DVCS data on a transversely polarized target [38, 39] is also shown together with lat-

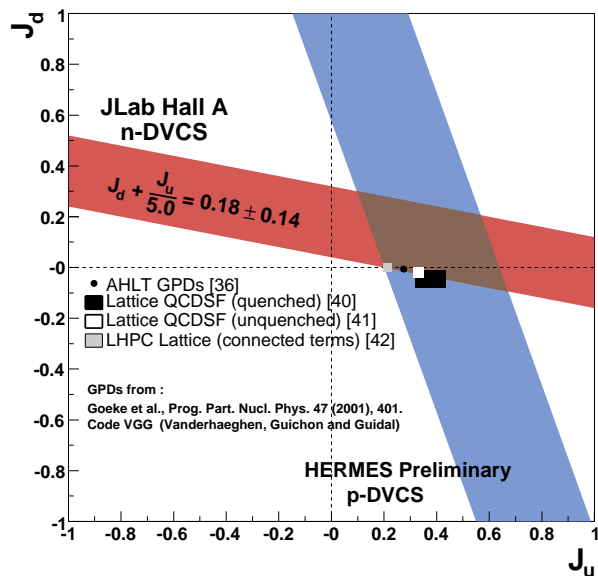


FIG. 4: Experimental constraint on J_u and J_d quark angular momenta from the present n-DVCS results. A similar constraint from the \bar{p} -DVCS target spin asymmetry measured by HERMES [38, 39], and different lattice QCD based calculations [36, 40, 41, 42] are also shown.

tice QCD based predictions [36, 40, 41, 42]. It remains a future theoretical study to evaluate, in a model independent way, the constraints on J_u and J_d from a finite set of measurements. As expected from isospin symmetry, n-DVCS data have enhanced sensitivity to the d quark of the proton relative to p-DVCS data. This complementarity is a key feature for future experimental programs investigating quark angular momenta.

In summary, this experiment provides a determination of the t -dependence of a linear combination of GPDs from the n-DVCS helicity-dependent cross-section difference in the range $[-0.5; -0.1]$ GeV². These data, mostly sensitive to E_q , were found to be compatible with zero. The coherent d-DVCS contribution was also extracted, the high $|t|$ behaviour being compatible with expectations. We provide the first experimental constraint on the parametrization of the GPD E_q that can be expressed, within a particular model, in terms of a constraint on the quark angular momenta. DVCS experiments on the neutron appear as a mandatory step towards a better knowledge of the partonic structure of the nucleon.

We acknowledge essential work of the JLab accelerator staff and the Hall A technical staff. This work was supported in part by DOE contract DOE-AC05-06OR23177 under which the Jefferson Science Associates, LLC, operates the Thomas Jefferson National Accelerator Facility, the National Science Foundation, the French CEA and IN2P3-CNRS.

- [1] R. Hofstadter, R.W. McAllister, Phys. Rev. **98**, 217 (1955).
- [2] M. Breidenbach et al. Phys. Rev. Lett. **23**, 935 (1969).
- [3] J. Ashman et al., Nucl. Phys. **B 328**, 1 (1989).
- [4] S.S. Adler et al., Phys. Rev. Lett. **93**, 202002 (2004).
- [5] S. Ageev et al., Phys. Lett. **B 633**, 25 (2006).
- [6] D. Mueller et al., Fortschr. Phys. **42**, 101 (1994).
- [7] A. V. Radyushkin, Phys. Rev. **D 56**, 5524 (1997).
- [8] X. Ji, Phys. Rev. Lett. **78**, 610 (1997).
- [9] M. Burkardt, Phys. Rev. **D 62**, 071503(R) (2000).
- [10] J.P. Ralston, B. Pire, Phys. Rev. **D 66**, 111501(R) (2002).
- [11] M. Diehl, Eur. Phys. J. **C 25**, 223 (2002).
- [12] A.V. Belitsky, D. Mueller, Nucl. Phys. **A 711**, 118c (2002).
- [13] M. Burkardt, Phys. Rev. **D 72**, 094020 (2005).
- [14] X. Ji, J. Osborne, Phys. Rev. **D 58**, 094018 (1998).
- [15] J.C. Collins, A. Freund, Phys. Rev. **D 59**, 074009 (1999).
- [16] M. Diehl et al., Phys. Lett. **B 411**, 193 (1997).
- [17] A.V. Belitsky et al., Nucl. Phys. **B 629**, 323 (2002).
- [18] A. Airapetian et al., Phys. Rev. Lett. **87**, 182001 (2001).
- [19] S. Stepanyan et al., Phys. Rev. Lett. **87**, 182002 (2001).
- [20] C. Adloff et al., Phys. Lett. **B 517**, 47 (2001).
- [21] S. Chekanov et al., Phys. Lett. **B 573**, 46 (2003).
- [22] A. Aktas et al., Eur. Phys. J. **C 44**, 1 (2005).
- [23] S. Chen et al., Phys. Rev. Lett. **97**, 072002 (2006).
- [24] A. Airapetian et al., Phys. Rev. **D 75**, 011103 (2007).
- [25] C. Muñoz Camacho et al., Phys. Rev. Lett. **97**, 262002 (2006).
- [26] P.-Y. Bertin, C.E. Hyde-Wright, F. Sabatié, E. Voutier et al., JLab Proposal **E03-106** (2003).
- [27] A. Alcorn et al., Nucl. Inst. and Meth. **A 522**, 294 (2004).
- [28] M. Mazouz, Thèse de Doctorat, Université Joseph Fourier, Grenoble (France), 2006.
- [29] M. Lacombe et al., Phys. Rev. **C 21**, 861 (1980).
- [30] A. Bacchetta et al., Phys. Rev. **D 70**, 117504 (2004); we follow the Trento convention for the definition of the azimuth $\phi_{\gamma\gamma}$ of the real photon q' around the q -direction.
- [31] A. Kirchner, D. Müller, Eur. Phys. J. **C32**, 347 (2004).
- [32] K. Goeke et al., Prog. Part. Nucl. Phys. **47**, 401 (2001).
- [33] M. Vanderhaeghen et al., Phys. Rev. **C 62**, 025501 (2000).
- [34] F. Cano, B. Pire, Eur. Phys. J. **A 19**, 423 (2004).
- [35] E.R. Berger et al., Phys. Rev. Lett. **87**, 142302 (2001).
- [36] S. Ahmad, H. Honkanen, S. Liuti, S.K. Taneja, Phys. Rev. **D 75**, 094003 (2007); ArXiv:hep-ph/0708.0268.
- [37] M. Vanderhaeghen, P.A.M. Guichon, M. Guidal, Phys. Rev. **D 60**, 094017 (1999).
- [38] F. Ellinghaus et al., Eur. Phys. J. **C 46**, 729 (2006).
- [39] Z. Ye, Proc. of the XIVth International Workshop on Deep Inelastic Scattering, Tsukuba (Japan), April 20-24, 2006; ArXiv:hep-ex/0606061.
- [40] M. Göckeler et al., Phys. Rev. Lett. **92**, 042002 (2004).
- [41] G. Schierholz, Proc. of the Workshop on Exclusive Reactions at High Momentum Transfer, Jefferson Lab, Newport News (USA), May 21-24, 2007.
- [42] Ph. Hägler et al., ArXiv:hep-lat/0705.4295.